

Article

Analysis of Factors Influencing Measurement Accuracy for High-Temperature Liquid Metal Flow Sensors in Nuclear Power

Gang Wang^{1,2}, Wenyi Lin¹, Yutao Jiang¹, Lixin Deng² and Yi Chai^{1,*} 

¹ College of Automation, Chongqing University, Chongqing 400044, China; wgang0519@163.com (G.W.); 20144253@cqu.edu.cn (W.L.); 20211301019@stu.cqu.edu.cn (Y.J.)

² Chongqing Chuanyi Automation Co., Ltd., Chongqing 400044, China; dlixin2023@163.com

* Correspondence: chaiyi@cqu.edu.cn

Abstract: Permanent magnet metal flowmeters are implemented to monitor the flow of liquid metal coolant in a nuclear reactor, whose measurement accuracy plays a significant role to ensure the safety and normal operation of the nuclear reactor. According to a theoretical analysis of the permanent magnet metal flowmeter, several factors such as temperature, nonlinear degree, and zero potential will affect the accuracy of measuring the flow. However, for a heavy-caliber permanent magnet metal flowmeter, the influence of the magnetic Reynolds number provides obvious nonlinearity, which affects the measurement accuracy of the flowmeter. Consequently, we use the finite element method to calculate the magnetic field of the flowmeter and analyze the cause of the nonlinearity. Additionally, the influence of nonlinear error is significantly reduced by designing the structure of the flowmeter and the appropriate arrangement of the electrodes.

Keywords: permanent magnet metal flowmeter; measurement accuracy analysis; magnetic field analysis; structural optimization; finite element analysis



Citation: Wang, G.; Lin, W.; Jiang, Y.; Deng, L.; Chai, Y. Analysis of Factors Influencing Measurement Accuracy for High-Temperature Liquid Metal Flow Sensors in Nuclear Power.

Electronics **2023**, *12*, 2944. <https://doi.org/10.3390/electronics12132944>

Academic Editor: Ahmed Abu-Siada

Received: 19 May 2023

Revised: 28 June 2023

Accepted: 29 June 2023

Published: 4 July 2023



Copyright: © 2023 by the authors. Licensee MDPI, Basel, Switzerland. This article is an open access article distributed under the terms and conditions of the Creative Commons Attribution (CC BY) license (<https://creativecommons.org/licenses/by/4.0/>).

1. Introduction

As the most promising clean energy source, nuclear energy releases huge amounts of energy through nuclear fission. In the process of energy conversion, it does not produce the carbon dioxide gas that causes the greenhouse effect, which efficiently reduces the harm to the environment. Since the first nuclear power plant was built in the former Soviet Union in 1954 and reached criticality, nuclear power plants have continued to develop. Meanwhile, different setups were investigated such as light water reactors, heavy water reactors, sodium-cooled nuclear reactors [1], gas-cooled nuclear reactors, and so on. After more than half a century of development, nuclear energy has become one of the major energy sources all over the world and may maintain its role in power generation for decades to come [2]. However, the development of nuclear energy may lead to the accumulation of nuclear waste. As a result, its improper operation may be detrimental to the natural environment [3,4].

The technology roadmap for the nuclear energy systems of the fourth-generation nuclear reactors was published by GIF, in which the nuclear system of the fast nuclear reactor is designed with an accelerator driven subcritical system (ADS). The produced neutrons can also transmute the high-level nuclear waste for the proliferation and production of nuclear fuel [5–7]. Therefore, the fast nuclear reactor provides technical advantages such as efficient utilization of uranium fuel resources and transmutation of long-lived radioactive waste from nuclear power plants, which can effectively solve the problems of nuclear fuel resource shortage and nuclear waste disposal. In recent years, it has gradually gained the attention of countries around the world [8–10].

The ADS designed in the fourth-generation nuclear power plants for fast nuclear reactors has proposed molten salt ADS, molten alloy ADS, sodium-cooled ADS, and

lead–bismuth alloy (LBE)-cooled ADS [11–13]. Among them, liquid metal is widely utilized as a coolant material in engineering due to its good thermal conductivity, neutron performance, irradiation resistance, and high heat transfer [14,15]. Generally, temperatures above 200 °C are regarded as the high-temperature state of the liquid metal. Moreover, in order to ensure the smooth operation of the reactor, it is necessary to monitor the coolant flow rate of each circuit in the ADS, so the appropriate flow measurement technology and equipment are required. Consequently, how to accurately measure the flow rate of liquid metals is one of the key technologies to ensure the stable operation of the equipment, and the flow measurement techniques for various liquid metal materials have become one of the most popular research projects in the nuclear energy field [16,17].

The liquid metal flowmeter applied in the nuclear power fields is one of the most important measurement instruments of the fourth-generation advanced nuclear power system. Due to the high temperature and high radiation during the operation of liquid metal, conventional flowmeters used in the industry cannot be directly used in this special condition. At present, the types of flowmeters studied on high-temperature liquid metal flow measurements include electromagnetic flowmeters, turbine flowmeters, gyrometer flowmeters, vortex flowmeters, orifice flowmeters, and ultrasonic flowmeters [18]. These various flowmeters have their advantages and disadvantages. The turbine flowmeter applies the principle of momentum for the measurement, which provides high accuracy. However, the components in the pipeline are easily damaged and provide poor stability. Gu et al. [19] designed an optical fiber turbine flowmeter based on the traditional turbine flowmeter, which reduces the lower limit of measurement and improves the measurement sensitivity. A gyrometer flowmeter that uses the Coriolis principle for measurement is insensitive to the measuring medium, but the temperature of the measuring medium is limited. A vortex flowmeter uses the Karman vortex street principle to measure low velocities, while it has requirements on the flow characteristics and Reynolds number of the metal liquid. Venugopal et al. [20] proposed a vortex flowmeter which improved the sensitivity of small flow measurements by many times. An orifice flowmeter uses the principle of pressure difference for the measurement, which contains a large error and may cause a large pressure loss in the pipeline. Moreover, the ultrasonic flowmeter uses the principle of acoustic wave propagation to measure, but it faces the problem of temperature resistance of the sensor probe. Ren et al. [21] designed a high-precision ultrasonic flowmeter based on the cross-correlation method. Weathered et al. [22] designed a permanent magnet flowmeter for a sodium fast reactor. Yu et al. [23] proposed an in situ calibration method for a permanent magnet sodium flowmeter, which provides high measurement accuracy.

However, an electromagnetic flowmeter has several advantages such as a simple structure, being non-contact, a strong output signal, good linearity at small diameters, high temperature resistance, and insensitivity to fluid flow characteristics compared to the above flowmeter types. Therefore, it is one of the main pieces of equipment for metal flow measurements at present [24]. According to the way of producing the working magnetic field, the types of electromagnetic flowmeter can be divided into coil excitation and permanent magnet. The coil excitation type can control the working magnetic field intensity by adjusting the excitation current, thereby achieving direct current and alternating current excitation. However, a strong magnetic field requires a large amount of current to excite it. Due to the resistance loss in the excitation coil, a large amount of heat energy is generated, which may cause the coil resistance to increase, insulation to decrease, and even lead to core melting. Therefore, sufficient heat dissipation is required for the coil to ensure normal operation. Permanent magnet excitation mode can generate a strong magnetic field through permanent magnet materials, which have a simpler structure than coil excitation. However, due to the decrease in magnetic properties of permanent magnet materials during use, regular calibration is required. At present, permanent magnet electromagnetic flowmeters are mainly used for metal flow measurements.

2. Measurement Principle

The permanent magnet metal flowmeter measures the flow of the metal medium in the pipeline based on Faraday’s law of electromagnetic induction. Therefore, when a liquid metal flows in a pipeline perpendicular to the magnetic field, it cuts magnetic field lines and generates an induced electromotive force on two electrodes perpendicular to the direction of movement and the magnetic field line direction of the liquid metal. The velocity of the liquid metal in the pipeline is calculated by measuring the size of induced electromotive force [25,26]. The induced electromotive force U is given by [27]

$$U = Bdv \tag{1}$$

where B (unit: T) is the magnetic flux density on the section of the pipe section, and d (m) and v (m/s) represent the pipe’s inside diameter and the flow velocity of the metal, respectively.

The general structure of the permanent magnet flowmeter is shown in Figure 1. The magnetic circuit is composed of a magnetic yoke, magnetic pole plate, and magnetic steel. Magnetic steel is the permanent magnet material and provides the working magnetic field inside the pipeline. The top signal electrode and bottom signal electrode are welded onto the pipe. The direction of the magnetic field, medium flow direction, and electrode line direction are perpendicular to each other, which is used to measure the induced electromotive force generated when the medium cuts the magnetic field in the pipe.

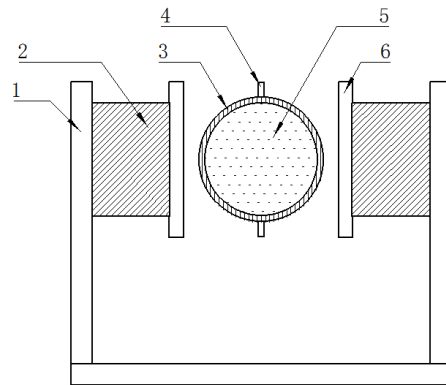


Figure 1. Structure of permanent magnet flowmeter: 1. magnet yoke, 2. magnetic steel, 3. pipeline, 4. electrode, 5. medium, 6. magnetic pole plate.

3. Measurement Accuracy Analysis

Fixing the liquid metal temperature, the induced electromotive force at the top and bottom electrodes can be expressed as [16]

$$U = Bdv \cdot K_1 \cdot K_2 \cdot K_3 \cdot K_4 \tag{2}$$

where U (V) denotes the induced electromotive force generated in the liquid metal, B (T) is the magnetic flux density on the section of the pipe section, d (m) and v (m/s) represent the pipe’s inside diameter and the flow velocity of the metal, respectively, and $K_1, K_2, K_3,$ and K_4 are the correction coefficients.

Specifically, K_1 is the correction coefficient of the shunt effect on the metal pipe wall, which can be computed as follows [28]

$$K_1 = \frac{2d/D}{1 + (d/D)^2 + (\rho_f/\rho_{ss}) [1 - (d/D)^2]} \tag{3}$$

where d (m) and D (m) are the inside diameter and outer diameter of the metal pipe, and ρ_f ($\Omega\cdot\text{cm}$) and ρ_{ss} ($\Omega\cdot\text{cm}$) are defined as the resistivity of the liquid metal and pipe, respectively.

K_2 is the correction coefficient of the shunt effect at the end of the magnetic pole, which is given by the ratio of the polar face length L to the inside diameter d .

K_3 is the correction coefficient for the decrease in the magnetic flux density caused by the increase in the magnetic steel temperature, and it is given by [28]

$$K_3 = 1 + \alpha_0(T_{cg} - T_0) \quad (4)$$

where α_0 ($\%/^{\circ}\text{C}$) represents the reversible temperature coefficient of magnetic steel, T_{cg} ($^{\circ}\text{C}$) corresponds to the temperature of magnetic steel in the working conditions, and T_0 ($^{\circ}\text{C}$) is the indoor temperature.

K_4 is the correction coefficient of the metal pipe's thermal expansion and can be obtained as follows [28]

$$K_4 = 1 + \alpha_1(T_{ss} - T_0) \quad (5)$$

where α_1 ($1/^{\circ}\text{C}$) is the thermal expansion coefficient of the conduit material and T_{ss} ($^{\circ}\text{C}$) denotes the temperature of the stainless steel pipe. It is generally considered that the temperature of the metal pipe is equal to that of the liquid metal when the liquid metal flows through the metal pipe.

By analyzing the above formulas, the factors affecting the measurement accuracy of high-temperature liquid metal flow sensors can be summarized as follows.

- (1) Temperature effect: According to Equation (2), in addition to d , B , and v , the induced electromotive force is related to the conductivity of the resistivity, the pipe size, the magnetic field distribution, and the temperature. The resistivity, pipe size, and magnetic properties of magnetic steel change with temperature, which affects the output characteristics of the sensor. Furthermore, the thermal expansion caused by temperature change may lead to the position of the signal electrode shifting and affect the signal strength of the electrode. The temperature increase in the magnetic steel caused by temperature diffusion of the metal medium may cause the stability of the magnetic steel to decrease, resulting in irreversible demagnetization.
- (2) Nonlinearity effect: From Equation (2), it can be seen that U is directly proportional to v and the characteristic curve of the permanent magnet metal flowmeter is linear when the coefficients K_1 , K_2 , K_3 , and K_4 are fixed. However, Equation (2) only considers the correction coefficient of the shunt effect at the end of magnetic pole K_2 , and does not consider the effect of the induced magnetic field which is generated by the induced current of the shunt effect at the end of the magnetic pole on the magnetostatic field. However, this is the main reason that the characteristic curve of a permanent magnet metal flowmeter is nonlinear. The influence quantity of the magnetostatic field can be described by the magnetic Reynolds number. In magnetohydrodynamics, the magnetic Reynolds number is defined as [25],

$$R_m = \mu\sigma vd \quad (6)$$

where μ (H/m) is the permeability of the liquid metal, whereas the magnetic constant is $4\pi \times 10^{-7} \text{H/m}$, σ (S/m) represents the conductivity of the liquid metal, v (m/s) is the average velocity of the liquid metal in the pipe, and d (m) is the characteristic length, which usually takes the inside diameter of the pipe.

The induced current in the pipe will produce an induced magnetic field, whose direction is determined by the right-hand spiral rule, so that the original magnetic field will be distorted. The induced current in the upstream, which generates a magnetic field opposite to the magnetostatic field, weakens the magnetostatic field. On the contrary, the induced current at downstream which generates the same magnetic field as the magnetostatic field, enhances the magnetostatic field. Finally, a new steady magnetic field is formed, as shown in Figure 2. Figure 2a shows the static magnetic field distribution of the permanent magnet flowmeter. Figure 2b represents the current density vector diagram of the permanent magnet flowmeter in the pipeline under the condition of medium flow. In this study, the finite element method is used to model, analyze, and calculate the characteristics of the sensor.

The steps are as follows. (1) Build the simulation model according to the design size. (2) Set the simulation parameters of each component according to the material properties of each component. (3) Add the physical field required for the simulation's calculations and set the parameters. (4) Construct a computing grid and solver for the simulation's calculations. In this way, the simulation results of a permanent magnet liquid metal flowmeter analyzed by finite element software are obtained. That is to say, the steady-state magnetic field distribution of a permanent magnet flowmeter under the influence of an induced magnetic field, which is shown in Figure 2c.

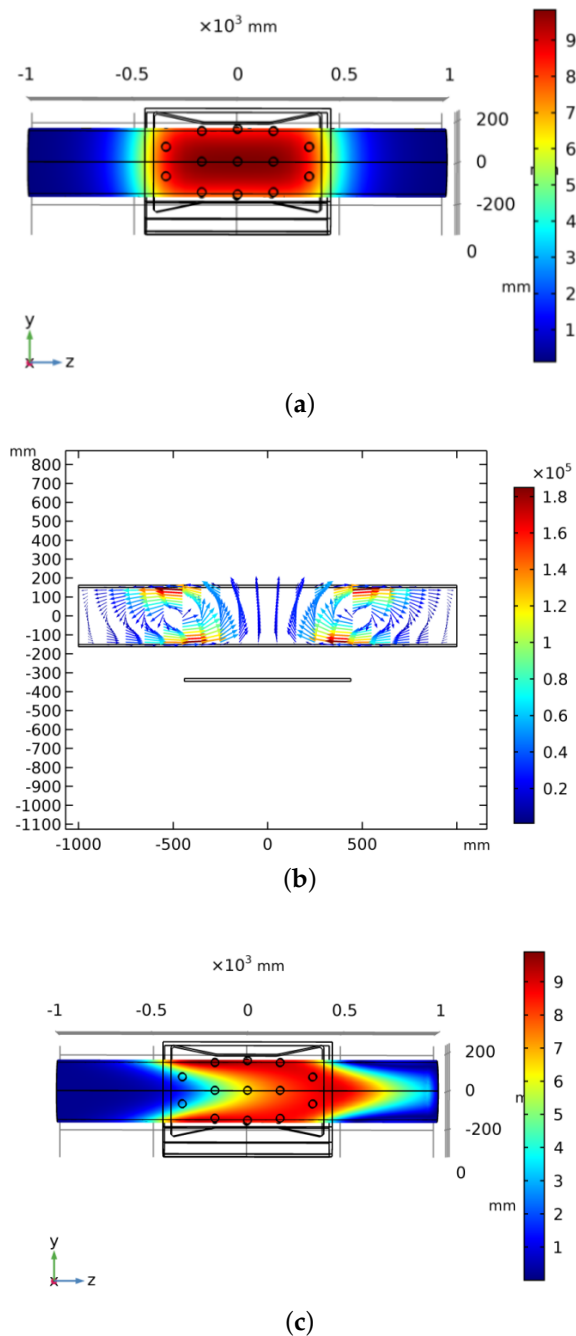


Figure 2. Magnetic field distribution and current density of permanent magnet flowmeter. (a) Magnetostatic field; (b) Electric current density; (c) Magnetic field distribution in the pipe at 8 m/s.

The basic equation of magnetic induction in the permanent magnet metal flowmeter is obtained from Maxwell's equations and the differential form of Ohm's law, as shown in Equations (7) and (8) [26].

$$\begin{cases} \nabla \cdot \vec{D} = \rho \\ \nabla \cdot \vec{B} = 0 \\ \nabla \times \vec{E} = -\frac{\partial \vec{B}}{\partial t} \\ \nabla \times \frac{\vec{B}}{\mu} = \vec{j} \end{cases} \quad (7)$$

$$\vec{j} = \sigma(\vec{E} + \vec{v} \times \vec{B}) \quad (8)$$

where \vec{D} is the electric displacement, ρ denotes the free charge density, \vec{E} represents the electric field intensity, μ and \vec{v} are the permeability and the velocity of the medium respectively, j is defined as the pipe current density in the permanent magnet metal flowmeter, and \vec{B} is the electric field, which is the static electric field generated by the accumulated charge caused by the Lorentz term $\vec{v} \times \vec{B}$.

When the charge in the conducting medium moves in the magnetic field, because of the action of the Lorentz force, it moves in the direction of the cross product of the velocity and the magnetic field vector, and the charge accumulates on the pipeline to form the electrostatic field \vec{E} . Since the Lorentz term is proportional to E , let the ratio of E to the Lorentz term be k , which is related to the size of the sensor structure, the conductivity of the pipe, and the metal medium. The value of k can be roughly estimated according to the shunt effect of the metal pipe wall and that of the end of the magnetic pole. Then, \vec{E} can be obtained by

$$\vec{E} = -k(\vec{v} \times \vec{B}) \quad (9)$$

Specifically, when the conductivity of the pipe and medium is infinite, the current density in the pipe is 0, and then k is 1. On the contrary, when the conductivity of the pipe and medium is infinite, no charge accumulates, and then $k = 0$. By transforming Equations (7)–(9), the follow formula is obtained as

$$\nabla \times \frac{\vec{B}}{\mu} = \vec{j} = \sigma(1 - k)(\vec{v} \times \vec{B}) \quad (10)$$

Then, integrate the closed path l based on Equations (7)–(10), as follows

$$\int_l B_1 dl = \int_s \mu \sigma v B \cdot (1 - k) ds \quad (11)$$

In this way, the expression of induced magnetic field 1, generated by the induced current, can be further obtained as

$$B_1 = \mu \sigma v B \cdot (1 - k) \cdot d \quad (12)$$

where d is the characteristic length, which usually takes the inside diameter of the pipe.

The influence of induced current on the static magnetic field can be expressed by the ratio of B_1 to B , as follows

$$\eta = \frac{B_1}{B} = \mu \sigma v d \cdot (1 - k) \quad (13)$$

From Equation (13), it can be seen that the magnetic Reynolds number R_m can qualitatively represent the influence of the induced current on the static magnetic field. If $R_m \ll 1$, the influence of the induced current on the static magnetic field can be ignored. If $R_m \gg 1$, the magnetic field distribution is affected by the induced magnetic field.

On the other hand, the basic equation of magnetic induction in magnetohydrodynamics can be obtained from Maxwell's equations (Equation (7)), and the differential form of Ohm's law (Equation (8)), as follows [29]

$$\frac{\partial \vec{B}}{\partial t} = \nabla \times (\vec{v} \times \vec{B}) + \frac{1}{\mu \cdot \sigma} \nabla^2 \vec{B} \quad (14)$$

If $R_m \ll 1$, Equation (14) is transformed into the following diffusion equation

$$\frac{\partial \vec{B}}{\partial t} = \frac{1}{\mu \cdot \sigma} \nabla^2 \vec{B} \quad (15)$$

Moreover, if $R_m \gg 1$, Equation (14) is transformed into the following freezing equation, and the plasma exhibits a magnetic freezing effect.

$$\frac{\partial \vec{B}}{\partial t} = \nabla \times (\vec{v} \times \vec{B}) \quad (16)$$

In this case, the induced magnetic field formed by the liquid metal flow is the main factor that causes the change in the static magnetic field. Considering this effect, the static magnetic field distribution shifts to the downstream direction of the flow, resulting in the nonlinear characteristic curve of the permanent magnet metal flowmeter. Since there is no external electric field during the operation of the permanent magnet metal flowmeter, the magnetic field change in the permanent magnet metal flowmeter is only caused by the induced magnetic field generated by the flow of the metal liquid.

- (3) Zero potential effect: At high temperatures, the signal electrode will produce the pyroelectric effect, which is a phenomenon of electric current or charge accumulation when the electrons in the heated object move from a high-temperature region to a low-temperature region with a temperature gradient. This phenomenon will lead to measurement error, which is caused by the strong potential difference between the top signal electrode and the bottom signal electrode when the metal medium in the pipe is stationary. The main factors of the thermoelectric effect are as follows
- A. Due to the difference between the electrode material and electrode lead material, the internal electron concentrations are different. Therefore, the transfer of electrons due to the temperature differences when heated leads to contact thermoelectric potential. In the case of inconsistent top and bottom electrodes, the contact potential between the electrodes and the pipe is different, thereby causing a potential difference between the top and bottom electrodes. On the other hand, if the lead materials of the top and bottom electrodes are inconsistent, the contact potential between the electrode and the electrode lead will be different, resulting in a potential difference between the top and bottom electrodes.
 - B. Due to the temperature asymmetry at the top and bottom electrodes, the internal temperature of the material is inconsistent, which makes the electrons migrate in a directional manner, resulting in a temperature potential. In addition, when the temperatures at the top and bottom electrodes are inconsistent, the temperature potential of the top and bottom electrodes will be different and produce potential differences.
 - C. The change in the internal structure in the processing of the pipeline's electrode makes the transformation from austenite to martensite, thus causing the difference caused by processing. Moreover, although the high temperature of 1000 °C and air cooling during the welding process cannot cause the structural transformation of stainless steel, the possible introduction of new substances and oxidation will also cause differences in the materials.

4. Simulation Analysis

According to the above analysis in Section 3, the output potential of the sensor is nonlinear with the velocity of the medium when the influence of the magnetic Reynolds number of the sensor is non-negligible. The induced current is related to the conductivity of the pipe and the sodium solution, the intensity and distribution of the magnetic field, and the inner and outer diameters of the pipe. The generated induced magnetic field and static magnetic field interact and iterate, and finally form a steady state. Specifically, iteration means that the generated induced magnetic field and the static magnetic field synthesize a new magnetic field, in which a new induced magnetic field will be generated, and continue to interact until a stable state is formed. Therefore, the process is complicated. However, the characteristic curve of the sensor cannot be calculated accurately by a theoretical formula calculation, it can only be obtained by finite element simulation analysis [30]. The finite element method accurately describes the distribution of electric and magnetic fields in the device [31]. When designing the flowmeter in this work, the finite element simulation is used to analyze the characteristics of the sensor qualitatively. Then, the structural model is optimized to make the structural form of the sensor satisfy the performance requirements. Finally, manufacture and test verification are carried out according to the structure size obtained by the simulation. In this way, the accuracy of the design can be improved. A 150-caliber permanent magnet metal flowmeter is designed in this paper. The structure of the permanent magnet flowmeter is shown in Figure 1.

By simulating the ratio structure of different magnetic pole surface lengths L and catheter inner diameters d , the linear difference of the center electrode signals with different structures is analyzed, as shown in Figure 3. The purpose of using linear fitting is to compare the linearity difference of different signals. We use the sum of squared errors (SSE) to judge the linear relationship of regression and select the best model. Meanwhile, in order to measure the degree of linear fit between the actual data and the fitting line, we use the normalized SSE (SSE') to illustrate the fitting degree of the signal. The calculation formulas of SSE and SSE' are shown in Equations (17) and (18), respectively. The essence of this method is the same as that of SSE after the normalization of the different electrode signal data. The smaller the SSE' value, the smaller the error between the fitting value and the actual value, which reflects the degree of fitting between the actual data and the fitting line, and indicates the linearity of the signal. Consequently, the larger L/d , the better the linear fitting is, which will produce better signal linearity of the sensor.

$$SSE = \sum_{i=1}^n (y_i - \hat{y}_i)^2 \quad (17)$$

$$SSE' = \frac{SSE}{y_{\max}^2} = \frac{\sum_{i=1}^n (y_i - \hat{y}_i)^2}{y_{\max}^2} \quad (18)$$

where y_i is the actual value, y_{\max}^2 indicates the maximum value of the actual data, and \hat{y}_i denotes the fitted value.

When $L/d = 2.7$, the linearity difference of the potential signal at different electrode positions is shown in Figure 4. Figure 4 shows that the linearity at 100 mm downstream is better, which indicates that the simulation results are consistent with the theoretical analysis.

Therefore, the structure of $L/d = 2.7$ is selected and a 150-caliber permanent magnet metal flowmeter is manufactured based on the analysis results in Section 3. Table 1 shows the measured magnetic field and simulated magnetic field on the central axis of the produced sensor. It is obvious that the difference between the measured magnetic field and the simulated magnetic field is small, which means the magnetic field distribution of the permanent magnet metal flowmeter can be accurately calculated by simulation calculation.

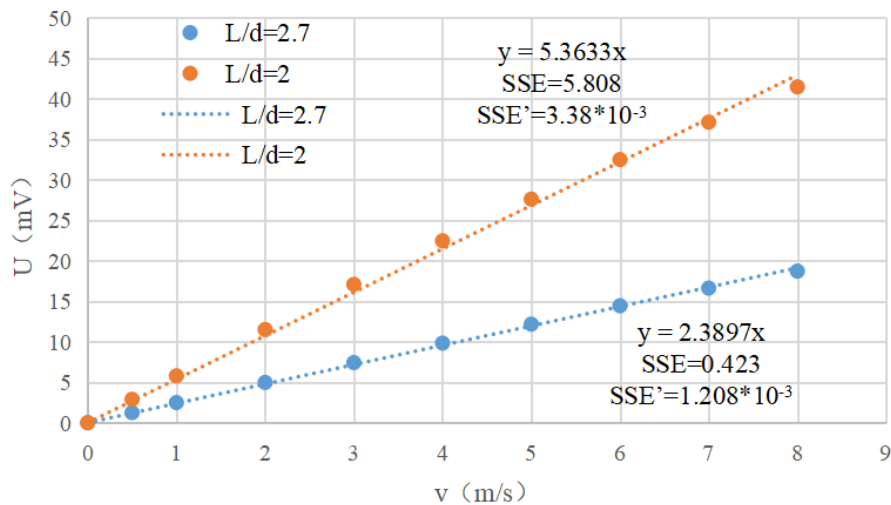


Figure 3. The difference in linearity of the center electrode signal at different L/d ratios.

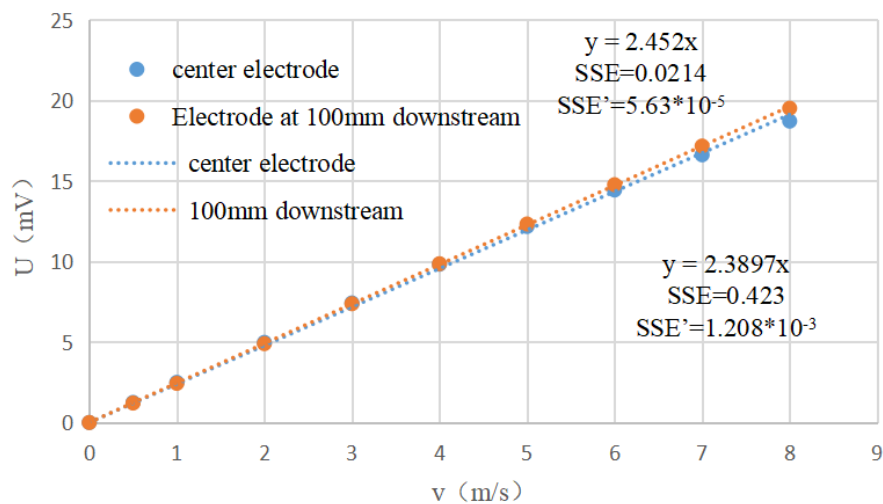


Figure 4. Linearity differences of potential signals at different electrode positions.

Table 1. Difference between measured magnetic field and simulated magnetic field on the central axis of the sensor.

Central Axis	50 mm Upstream	25 mm Upstream	0 mm Upstream (Pipe Center)	25 mm Downstream	50 mm Downstream
Simulated magnetic field (mT)	18.000	18.045	18.055	18.044	18.000
Measured magnetic field (mT)	18.000	18.050	18.050	18.020	17.990
Difference (%)	0.000	−0.028	0.028	0.133	0.056

Additionally, a hot metal measurement experiment is carried out with the 150-caliber permanent magnet metal flowmeter. The permanent magnet liquid metal flowmeter is installed on the calibration circuit, and the real flow calibration experiment is carried out by the dynamic volumetric method [32]. During the experiment, the potential signals of the central electrode and 100 mm downstream are collected and they are compared with the simulated potential, as shown in Table 2. During the test, the measured potential will be disturbed by environmental factors, resulting in measurement errors. The maximum error between the measured potential and simulated potential is −1.51%. The size, material parameters, grid, and solver settings of the model during the simulation’s calculations may

cause calculation errors, so it is normal to have errors between the measured potential and the simulated potential.

Table 2. Difference between measured potential and simulated potential at different electrode positions.

Central Electrode				Electrode at 100 mm Downstream		
Flow Velocity (m/s)	Measured Potential (mV)	Simulated Potential (mV)	Error (%)	Measured Potential (mV)	Simulated Potential (mV)	Error (%)
0.779	1.891	1.920	−1.51	1.849	1.866	−0.91
1.420	3.493	3.533	−1.13	3.437	3.458	−0.61
2.344	5.777	5.811	−0.59	5.737	5.740	−0.05
3.120	7.663	7.683	−0.26	7.666	7.645	0.27
4.378	10.651	10.639	0.11	10.805	10.713	0.86

The signal output characteristics of the permanent magnet metal flowmeter can be calculated accurately by the simulation. The simulation can effectively guide the design of a permanent magnet metal flowmeter and reduce the influence of interference factors on the accuracy of the flow measurement.

5. Conclusions

Permanent magnet metal flowmeters are widely applied in the nuclear power field to measure high-temperature liquid metal flows. According to the theoretical analysis of the permanent magnet metal flowmeter, it can be seen that several factors affecting the accuracy of the flow measurement are temperature, the nonlinear degree, and the zero potential. All in all, the theoretical analysis, calculation, and experiment can be concluded as follows:

- (1) We qualitatively analyze and quantitatively calculate the interaction between the original magnetic field and the induced magnetic field of a permanent magnet metal flowmeter, which is the reason that causes the nonlinear characteristics of the flowmeter.
- (2) By selecting the appropriate ratio of magnetic pole surface length to the inner diameter of the flow tube, and placing the signal electrodes in the appropriate position, the nonlinear error of the flowmeter can be reduced.
- (3) The magnetic field measurement is conducted, which is consistent with the numerical simulation results, which proves the correctness of the magnetic field analysis. Moreover, real flow calibration and verification experiments are conducted on permanent magnet metal flowmeters and the experimental result indicates the effectiveness of the structural design and electrode placement.

Author Contributions: Conceptualization, G.W. and W.L.; methodology, G.W. and W.L.; software, Y.J.; validation, L.D. and Y.C.; formal analysis, W.L., Y.J. and L.D.; resources, G.W. and Y.C.; writing—original draft preparation, G.W. and W.L.; writing—review and editing, Y.J., L.D. and Y.C.; visualization, G.W.; supervision, L.D. and Y.C.; project administration, Y.C.; funding acquisition, Y.C. All authors have read and agreed to the published version of the manuscript.

Funding: This research was supported by the National Key Research and Development Project (No. 2020YFB2009204).

Conflicts of Interest: The authors declare no conflict of interest.

References

1. Nosov, Y.; Rovneiko, A.; Tashlykov, O.L.; Shcheklein, S. Decommissioning Features of BN-350, -600 Fast Reactors. *At. Energy* **2019**, *125*, 219–223. [[CrossRef](#)]
2. Afia, R.S.A.; Mustafa, E.; Ádám Tamus, Z. Mechanical and low-frequency dielectric properties of thermally and thermo-mechanically aged low voltage CSPE/XLPE nuclear power plant cables. *Electronics* **2021**, *10*, 2728. [[CrossRef](#)]
3. Chu, H.; Chang, Z.; Shao, Y.; Zhang, X.; Lloret, J. An array-type system applied to complex surfaces in nuclear pollution detection. *Electronics* **2020**, *9*, 1870. [[CrossRef](#)]

4. Tashlykov, O.L.; Alqahtani, M.S.; Mahmoud, K.A. The role of natural rock filler in optimizing the radiation protection capacity of the intermediate-level radioactive waste containers. *Nucl. Eng. Technol.* **2022**, *54*, 3849–3854. [[CrossRef](#)]
5. Stanculescu, A. Accelerator driven systems (ADSs) for nuclear transmutation. *Ann. Nucl. Energy* **2013**, *62*, 607–612. [[CrossRef](#)]
6. Wallenius, J. Maximum efficiency nuclear waste transmutation. *Ann. Nucl. Energy* **2019**, *125*, 74–79. [[CrossRef](#)]
7. Chen, Z.; Wu, Y.; Yuan, B.; Pan, D. Nuclear waste transmutation performance assessment of an accelerator driven subcritical reactor for waste transmutation (ADS-NWT). *Ann. Nucl. Energy* **2015**, *75*, 723–727. [[CrossRef](#)]
8. Du, X.; Ye, Q.; Xu, M.; Wan, Y.; Peng, X.; Su, G.; Yang, Y.; Gao, X.; Shi, X. Research on technology directions and development roadmap of nuclear energy. *Eng. Sci.* **2018**, *20*, 17–24. [[CrossRef](#)]
9. He, J.; Guo, Z. Development status of sodium cooled fast reactor. *Dongfang Electr. Rev.* **2013**, *27*, 36–43.
10. Wang, L. Experimental Study on Thermophysical Properties of Lead Bismuth Alloys for Advanced Nuclear Reactor. Master's Thesis, Hefei University of Technology, Hefei, China, 2014.
11. Shi, C.; Cheng, M.; Liu, G. Development and application of a system analysis code for liquid fueled molten salt reactors based on RELAP5 code. *Nucl. Eng. Des.* **2016**, *305*, 378–388. [[CrossRef](#)]
12. Li, S.; Cao, L.; Khan, M.S.; Chen, H. Development of a sub-channel thermal hydraulic analysis code and its application to lead cooled fast reactor. *Appl. Therm. Eng.* **2017**, *117*, 443–451. [[CrossRef](#)]
13. Lu, Y.; Zhu, R.; Fu, Q.; Wang, X.; An, C.; Chen, J. Research on the structure design of the LBE reactor coolant pump in the lead base heap. *Nucl. Eng. Technol.* **2019**, *51*, 546–555. [[CrossRef](#)]
14. Yan, B. *Stainless Steel Manual*; Chemical Industry Press: Beijing, China, 2009.
15. Committee, O.N.S.; Rong, L. *Handbook on Lead-Bismuth Eutectic Alloy and Lead Properties, Materials Compatibility, Thermal-Hydraulics and Technologies*; Science Press: Beijing, China, 2014.
16. Rajan, K.K.; Vijayakumar, G. Stabilization of magnet assemblies of permanent magnet sodium flowmeters used in fast breeder reactors. *Nucl. Eng. Des.* **2014**, *275*, 368–374. [[CrossRef](#)]
17. Wu, H.; Jin, J.; Yang, J.; Dong, K. Design and verification of magnetic circuit for DN80 permanent-magnet sodium flow meter. *Sci. Technol. Vis.* **2018**, 2095–2457. [[CrossRef](#)]
18. Lu, Y. Design and Preliminary Calibration Test of PbBi Electromagnetic Flow-Meter. Master's Thesis, University of Science and Technology of China, Hefei, China, 2014.
19. Gu, Y.; Zhao, Y.; Lv, R.; Yang, Y. Theory and structure of a modified optical fiber turbine flowmeter. *Flow Meas. Instrum.* **2016**, *50*, 178–184. [[CrossRef](#)]
20. Arumuru, V.; Dash, J.N.; Dora, D.; Jha, R. Vortex shedding optical flowmeter based on photonic crystal fiber. *Sci. Rep.* **2019**, *9*, 8313. [[CrossRef](#)]
21. Ren, R.; Wang, H.; Sun, X.; Quan, H. Design and implementation of an ultrasonic flowmeter based on the cross-correlation method. *Sensors* **2022**, *22*, 7470. [[CrossRef](#)]
22. Weathered, M.; Grandy, C.; Anderson, M.; Lisowski, D. High temperature sodium submersible flowmeter design and analysis. *IEEE Sens. J.* **2021**, *21*, 16529–16537. [[CrossRef](#)]
23. Yu, X.; Xu, K.; Wu, W.; Huang, Y. Research on nonlinearity in in situ calibration of permanent magnet sodium flowmeter without bluff body. *IEEE Trans. Instrum. Meas.* **2021**, *70*, 7501114. [[CrossRef](#)]
24. Yang, Y.; Wang, D.; Niu, P.; Liu, M.; Wang, S. Gas-liquid two-phase flow measurements by the electromagnetic flowmeter combined with a phase-isolation method. *Flow Meas. Instrum.* **2018**, *60*, 78–87. [[CrossRef](#)]
25. Sharma, V.; Kumar, G.V.; Dash, S.K.; Nashine, B.K.; Rajan, K.K. Modeling of permanent magnet flowmeter for voltage signal estimation and its experimental verification. *Flow Meas. Instrum.* **2012**, *28*, 22–27. [[CrossRef](#)]
26. Tang, R. *Modern Permanent Magnet Machines Theory and Design*; China Machine Press: Beijing, China, 2016.
27. Chen, D. Development of permanent-magnet sodium flowmeter. *Nucl. Power Eng.* **1991**, *12*, 26–33.
28. Shercliff, J.A. *The Theory of Electromagnetic Flow-Measurement*; Cambridge University Press: Cambridge, UK, 1962.
29. Stieglitz, R.; Muller, U. Experimental demonstration of a homogeneous two-scale dynamo. *Phys. Fluids* **2001**, *13*, 561–564. [[CrossRef](#)]
30. Li, L.; Du, X.; Pan, J.; Keating, A.; Matthews, D.; Huang, H.; Zheng, J. Distributed magnetic flux density on the cross-section of a transformer core. *Electronics* **2019**, *8*, 297. [[CrossRef](#)]
31. Sun, K.; Shi, J.; Cui, W.; Meng, G. Theoretical computational model for cylindrical permanent magnet coupling. *Electronics* **2021**, *10*, 2026. [[CrossRef](#)]
32. Xu, Y. Types of flow standard devices (1). *China Metrol.* **2014**, *7*, 120–123. [[CrossRef](#)]

Disclaimer/Publisher's Note: The statements, opinions and data contained in all publications are solely those of the individual author(s) and contributor(s) and not of MDPI and/or the editor(s). MDPI and/or the editor(s) disclaim responsibility for any injury to people or property resulting from any ideas, methods, instructions or products referred to in the content.